2016-01-08

Dynamic fragmentation of cellular, ice-templated alumina scaffolds

Tan, Yi Ming

Journal of Applied Physics

http://hdl.handle.net/10945/51540

JOURNAL OF APPLIED PHYSICS **119**, 024901 (2016)

Dynamic fragmentation of cellular, ice-templated alumina scaffolds

Yi Ming Tan,[1] Octavio Cervantes,[2] SeanWoo Nam,[1] John D. Molitoris,[2] and Joseph P. Hooper[1,a)]
[1]*Department of Physics, Naval Postgraduate School, Monterey, California 93943, USA*
[2]*Lawrence Livermore National Laboratory, Livermore, California 94550, USA*

(Received 9 November 2015; accepted 28 December 2015; published online 8 January 2016)

We examine the dynamic failure of ice-templated freeze-cast alumina scaffolds that are being considered as biomimetic hierarchical structures. Three porosities of alumina freeze-cast structures were fabricated, and a systematic variation in microstructural properties such as lamellar width and thickness was observed with changing porosity. Dynamic impact tests were performed in a light-gas gun to examine the failure properties of these materials under high strain-rate loading. Nearly complete delamination was observed following impact, along with characteristic cracking across the lamellar width. Average fragment size decreases with increasing porosity, and a theoretical model was developed to explain this behavior based on microstructural changes. Using an energy balance between kinetic, strain, and surface energies within a single lamella, we are able to accurately predict the characteristic fragment size using only standard material properties of bulk alumina. © *2016 AIP Publishing LLC*. [http://dx.doi.org/10.1063/1.4939702]

I. INTRODUCTION

Freeze casting synthesis methods have been highly successful in producing porous materials with controlled microstructures and biomimetic properties.[1–5] Polymer, metal, and ceramic scaffolds have been produced; this is often followed by polymer or metal infiltration into the pore structure to create high-performance composites.[6–8] Deville *et al*. have done extensive work on the freeze casting of hydroxyapatite scaffolds for bone tissue engineering.[9] They report how freeze casting can be applied to synthesize porous scaffolds exhibiting unusually high compressive strength, e.g., up to 145 MPa for 47% porosity and 65 MPa for 56% porosity. Ceramic scaffolds with a polymer infiltration such as alumina-polymethylmethacrylate (Al_2O_3-PMMA) have also received particular attention as a synthetic composite with similarities to nacre.[6,7,10–14] The hierarchical polymer/ceramic layered structure leads to enhanced fracture toughness and failure strain compared to a monolithic structure of either component. Munch and coworkers discuss several apparent toughness enhancement mechanisms in the Al_2O_3-PMMA structure, including inelastic deformation of the polymer, frictional sliding between ceramic blocks, and bridges that span across a growing crack and carry additional load.[7] Several recent studies have explored the origin of these toughness enhancement mechanisms in these materials and their biological counterparts; Ref. 5 reviews many of these studies.

The majority of mechanical testing on freeze-cast Al_2O_3-PMMA composites has focused on quasistatic measurements of compressive strength, fracture toughness, or bending strength. Munch and coworkers report compressive strengths of approximately 100 MPa for lamellar alumina-PMMA structures; Han *et al*.[13] and Yoon *et al*.[12] report similar strengths for porosities close to 60%. While these compressive strengths are lower than would be anticipated from a rule-of-mixtures of the two components, they are able to achieve these strengths with significant increases in the strain-to-failure and fracture toughness. The measured plane-strain toughness K_{Ic} for the infiltrated lamellar structures is in the range 4 MPa$\sqrt{\text{m}}$, higher than either the ceramic or polymer components individually and nearly double what would be expected from a mixture rule of toughness values.[7] Considerable progress has also been made on controlled and templated growth of the lamellar layers using a patterned cold finger,[15] radial cooling,[16,17] bidirectional freezing,[18] applied magnetic fields,[19] and templated grain growth.[20] These methods have demonstrated the ability to tune the anisotropy and growth patterns of lamellae in freeze-cast materials, with corresponding changes in quasistatic strength and failure strain.

The mechanical behavior of these composites under high strain-rate or impact loading has received considerably less attention, but is a critical property for applications as a bone replacement or lightweight, energy absorbing material. Here, we consider a baseline porous alumina scaffold under intense impact loading as a foundation for understanding the more complex hierarchical composite, which may be infiltrated with a variety of polymers or metals. The alumina scaffold forms a complex interconnecting matrix of lamella with a largely open porosity, and our interest is in understanding the dynamic fracture and fragmentation of this porous structure directly. Three porosities of alumina freeze-cast structures were grown with an ice-solidification process, and the microstructural changes were analyzed as a function of changing porosity and growth conditions. Dynamic impact tests were performed in a light-gas gun to catastrophically fragment all samples at high rates of loading. Widespread delamination is observed, along with characteristic cracking across the lamellar width. We introduce an energy-balance

a)Electronic mail: jphooper@nps.edu

fragmentation model to explain the experimental fragment distributions; using only the properties of bulk alumina, we are able to successfully predict the average fragment size for freeze-cast materials with different microstructures.

II. SYNTHESIS

A series of three porosities of cellular freeze-cast materials were grown following the methodology in Refs. 6 and 7. Slurries were prepared consisting of distilled water, alumina powder alumina powder with average particle size 0.4 μm (Ceralox SPA-0.5, Sasol North America, Inc., Tucson, AR), ammonium polymethacrylate dispersant (Darvan CN, Vanderbilt Minerals, LLC, Norwalk, CT, typically 2 wt. %), and an organic binder (Aquazol 5, Polymer Chemistry Innovations, Inc., Tucson, AR, typically 3 wt. %). The amount of alumina powder and distilled water varied based on the desired porosity of the sample. The slurry was ball milled for approximately 24 h and then stirred in a desiccator until air bubbles were removed. Slurries were poured into a Teflon mold with a copper rod at the bottom. The copper rod was cooled using liquid nitrogen. Freezing proceeded from bottom up and was controlled by heaters on the copper rods. A constant cooling rate of 1 °C/min was applied in the production all of the samples. Frozen samples were then freeze-dried for 24 h. The resulting green bodies were sintered in air using a 5 °C/min heating rate to 1500 °C with a 2 h hold. The samples were then air cooled at a 5 °C per minute rate. After sintering, the average sample size was approximately 16 mm in diameter by 30 mm long.

III. RESULTS AND DISCUSSION

A. Morphology

The morphology of the cellular freeze-cast materials is closely related to the crystallographic and growth characteristics of ice. As the growth conditions are altered to adjust the sample porosity, we also observe systematic changes in the morphology of the lamella and pore channels, similar to previous reports. In Figure 1, we present low-magnification electron microscopy images (Zeiss Neon 40 field-emission SEM with a voltage of 2 kV) of a cross section of each porosity considered in this study: 46%, 60%, and 75%. The lamellae grow in the direction of the freezing front, but here (where no additional templating procedure is used) their orientations orthogonal to the freezing front are essentially random. To provide some quantification of the microstructural changes as a function of porosity, we analyzed six main characteristics using measurements over multiple SEM images: the alumina grain diameter, the size of porous channels between lamellae, the lamellar thickness, the width of lamellae perpendicular to the solidification front direction, the height of the dendritic surface ridges, and finally, the spacing between ridges on the surface of the lamella. A minimum of twenty measurements of each property were taken on six or more SEM images of each porosity level. Figures 2 and 3 summarize the dimensions measured in this way, with error bars marking the standard deviation of the measurements.

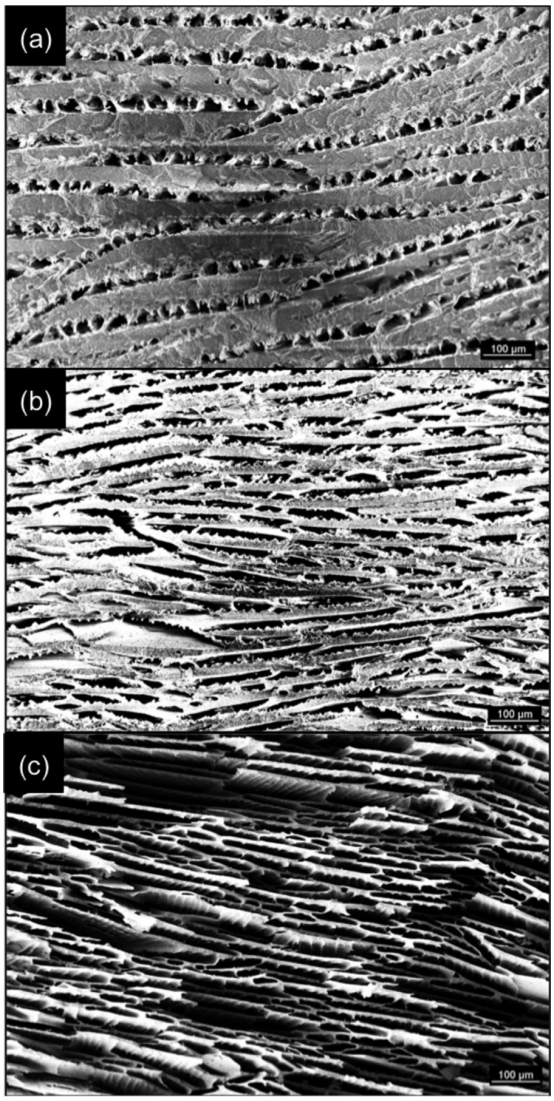

FIG. 1. Low-magnification electron microscopy of (a) 46%, (b) 60%, and (c) 75% porous samples.

At the grain level, lamella in all samples are similar; minimal residual porosity is observed and grains frequently exhibit terracing due to thermal etching from the sintering process. The surface of the lamellae contain dendritic features ranging from 3 to 12 μm high depending on the porosity level. The grain structure and dendritic features can be seen in Figure 4 and Figure S1 in the supplementary material[21] for fragments recovered from impact experiments.

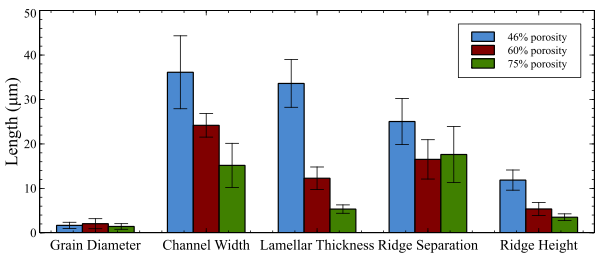

FIG. 2. Variation in microstructural characteristics with changing porosity.

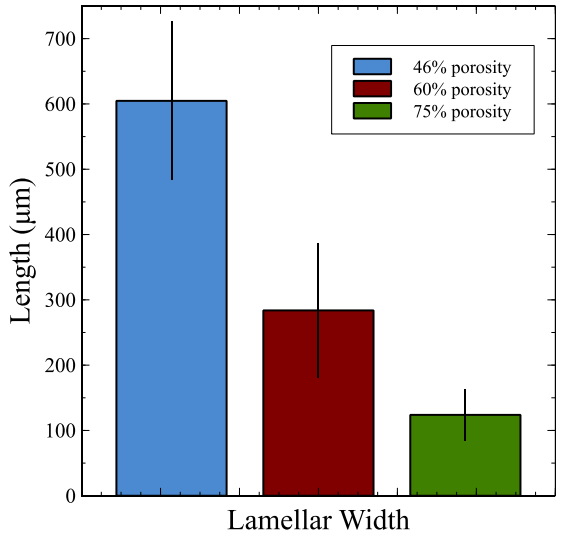

FIG. 3. Lamellar width for each sample considered in this study.

Consistent with previous literature, the dendritic surface features are found only on one side of the lamellae. The grain diameter for the three samples is consistent as expected, with an average diameter of 1.7 μm. In all other parameters measured (other than the distance between the ridges), we observe a trend in which the dimensional values decrease with increasing porosity. The width of the lamellae, for example, is defined as the distance between junctions or interfaces between lamellae and decreases rapidly with increasing porosity (Figure 2). The lamellar thickness and width in particular, given in Figures 2 and 3 and seen in the SEM image in Figure 1, both show a significant decrease moving from 46% to 75% porosity. No lamellar length is measured, but we have extracted SEM images of post-impact fragments and observed that the relative length of the lamellae is significantly greater than their width, consistent with previous reports. We note that all measurements were taken from cross-sections cut with a sectioning saw in the middle of the growth specimen. Previous reports have indicated some variation in microstructural properties along the vertical solidification direction, and we cannot fully observe this variation here.

Surface area was measured with a Brunauer-Emmett-Teller (BET) methodology using a Quantachrome Instruments Nova 4200e Surface Area and Pore Size Analyzer, measuring the nitrogen adsorption isotherm at 77 K. Before measurement, the samples were degassed at 300 °C for 2.5 h. The surface areas were obtained from the adsorption isotherms. Two runs were conducted for each sample to ensure consistency in

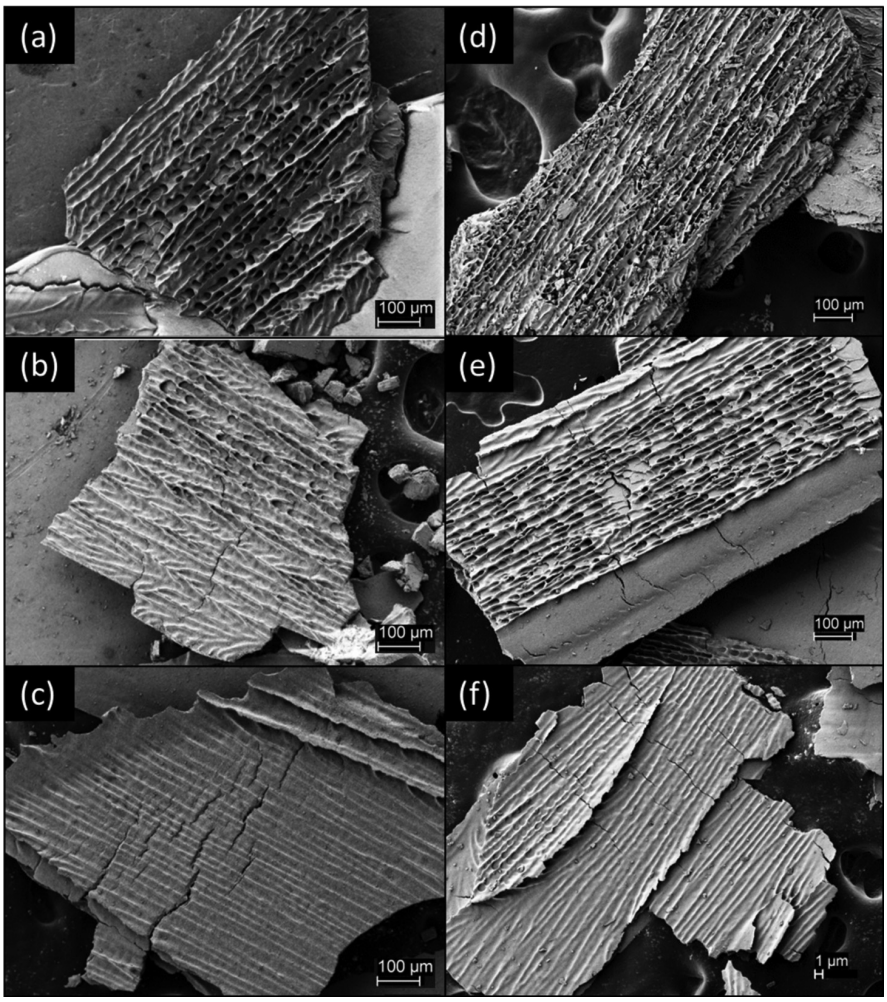

FIG. 4. Representative small fragments following impact.

TABLE I. BET surface area of all samples.

Porosity (%)	Average surface area (m^2/g)
46	0.638
60	0.889
75	1.423

the results. Table I summarizes the results for the samples. The average surface area results indicated that with increasing porosity the surface area also increases, as would be expected.

B. Impact experiments

To investigate the dynamic fracture of the freeze cast material, low velocity gas gun impact tests were conducted on cylindrical samples. Tests used a gun-propelled projectile in a 76 mm diameter light-gas gun to drive an intermediate striker bar into the sample, which rested on a rigid anvil. A schematic of the impact chamber is shown in Figure 5. The entire apparatus was contained within the gun catch chamber, which was pumped to a vacuum of 100 mTorr. The technique bears some similarities to Hopkinson bar impact or a dynamic Brazilian test, but allows for more severe impact conditions due to increased striker velocity. Unlike a traditional split Hopkinson bar test, the loading pulse from the striker is determined by a calibrated rubber insert around the striker bar that limits its maximum displacement. The deceleration profile of the striker bar was not measured, but the rubber insert was adjusted via multiple test shots so that its maximum displacement was 0.5 cm from the anvil face, corresponding to approximately 2/3 of the freeze-cast sample diameter. Here, a 480 g aluminum impactor was used to drive a 2.54 cm diameter steel striker bar into the freeze-cast sample. For fragment recovery shots, the impact velocity of the striker bar on the freeze cast sample was 39 ± 3 m/s; unlike Hopkinson bar loading, the intent here is simply to catastrophically fragment the sample rather than make dynamic measurements in a controlled stress state.

The sample fragments were fully contained within a chamber to allow for post-mortem recovery and analysis. The inner dimensions of the chamber were approximately 15 times larger than the sample dimensions to ensure fragments did not immediately strike an adjacent wall. However, we cannot completely exclude the possibility of some secondary fragmentation when initial fragments strike the catch container. Due to the vacuum required in the gun chamber, standard foams or gels used for soft-catch of brittle materials were problematic. The use of soft elastomers to line the chamber was also problematic, as small fragments are difficult to extract without additional damage and the polymer residue on fragments can complicate the sieving process. Thus, a chamber with as wide a diameter as possible was used to allow for some deceleration following initial impact.

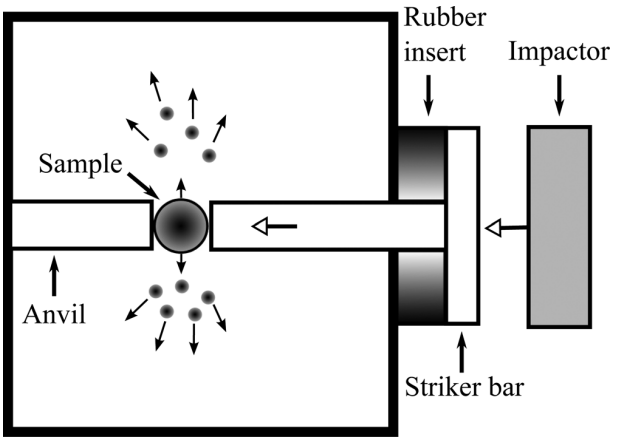

FIG. 5. Schematic of the impact chamber used to fragment the materials at high rates.

The as-cast materials were cylindrical with a diameter of 16 ± 0.2 mm. Samples for impact tests were made by cutting these cylinders to a reduced height while retaining the as-cast diameter. We note that due to edge effects, there is a slightly denser shell of lamellae on the exterior of this cylinder. Samples of differing porosities were cut to a height that yielded a specimen of approximately 3 g total mass. Due to the brittleness and porosity of the samples, achieving identical heights was challenging. The sample diameters were controlled by the growth apparatus and were much more uniform; this also presents the lamella to the impact in their most susceptible orientation. Samples were impacted across their diameter, with the lamellar growth direction perpendicular to the axis of impact. In the direction orthogonal to the impact, the lamellar orientation is more random. We thus expect the resulting fragmentation process to be an average of impacts over a range of different lamellar wall orientations. To account for variations in height and mass, all recovered fragment distributions were normalized to the total mass collected for a given shot. Each sample for fragmentation testing was bonded onto the anvil in the containment unit by a very small amount of epoxy, and the small mass of fragments that remained bound to the epoxy was not included in the results.

The fragments collected from the impact test were examined via SEM to observe relevant features of the dynamic fracture. All samples showed a number of consistent fracture behaviors. Widespread delamination was observed in recovered fragments, with failure typically occurring at the junctions between adjacent lamellae. On fractured lamellar strips, nearly all cracks propagated across the lamella width, orthogonal to the growth direction of the lamella. This was evident on the fragments where the broken edges were commonly perpendicular to the direction of the dendritic ridges, which run parallel to the direction of lamella growth. Figure 6 shows two typical surfaces of very large fragments from the 46% porosity sample where delamination occurred at the broken edges, and cracks were observed to be propagating across the lamellae.

Cracks have predominately an intergranular character, but transgranular fracture is also common especially in cases where the grain boundary makes a high angle with the crack path. Figure 7 shows a representative fracture surface exhibiting this mixed character; additional images are present in the supplementary material.[21] Grain bridging is commonly observed for these lateral cracks, similar to previous

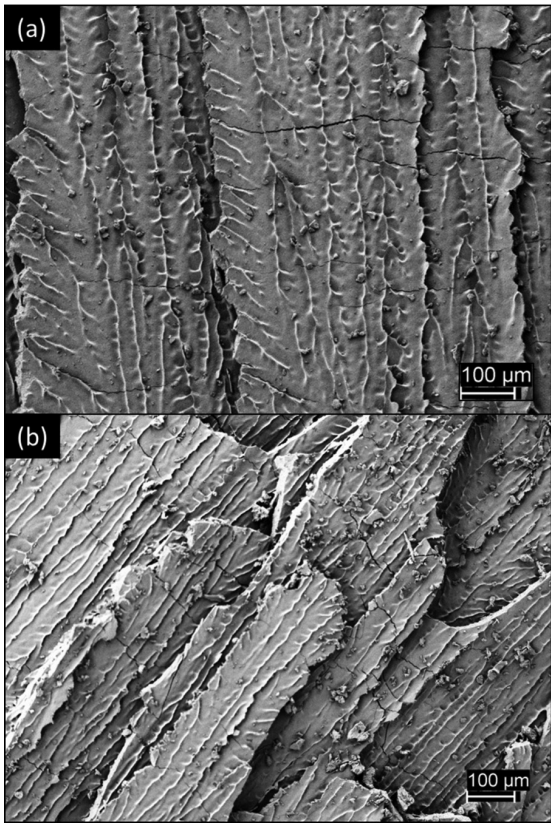

FIG. 6. SEM images of large recovered fragments following impact, showing delamination and incomplete lateral cracking across the lamellae.

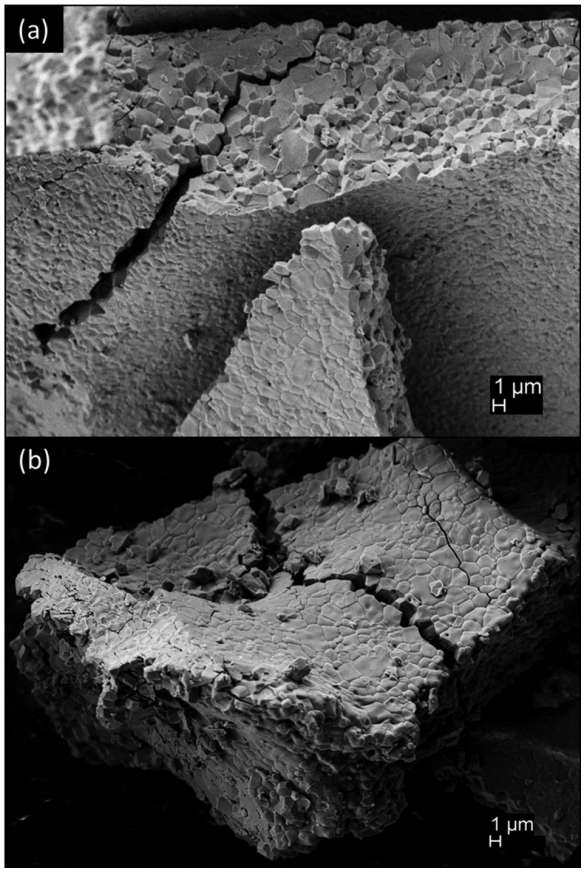

FIG. 7. Large recovered fragments showing crack features with a mix of trans- and intergranular character.

reports.[22] These fracture patterns are consistent with the large body of literature on fine-grained alumina.

C. Fragmentation results

Fragments were collected post-shot and carefully sieved with a standard sieve stack to determine their mass distribution as a function of a linear particle size. The contents of each sieve were weighed in a microbalance and converted to a mass probability density function distributed over linear size. A small amount of mass (between 2% and 4% for impacts presented here) was lost during the sieving process. The distributions for the three porosity levels are shown in Figure 8 with the 60% and 75% data shifted upwards for clarity. Solid lines are fits to a one-dimensional Lineau distribution discussed below. In all cases, a distinct maximum is observed at sizes below 200 μm, with the characteristic fragment size becoming smaller as porosity is increased. We note that the lamellar width and thickness also decrease with increasing porosity, and we will make use of this in the model below to explain the observed reduction in characteristic fragment size.

Based on the morphological features discussed above, we now consider a simple analytic model for the fragmentation of these ice-templated alumina structures under dynamic loading. We are interested both in predicting the fragment distribution and characteristic size, as well as accounting for the reduction in characteristic fragment size as the porosity increases. We consider two main points: the average fragment size and the overall shape of the mass probability density function. For the latter, we observe that many lamella detach at all junctions with other lamellae, leaving long sheet-like strips (typical examples are shown in Figure 4).

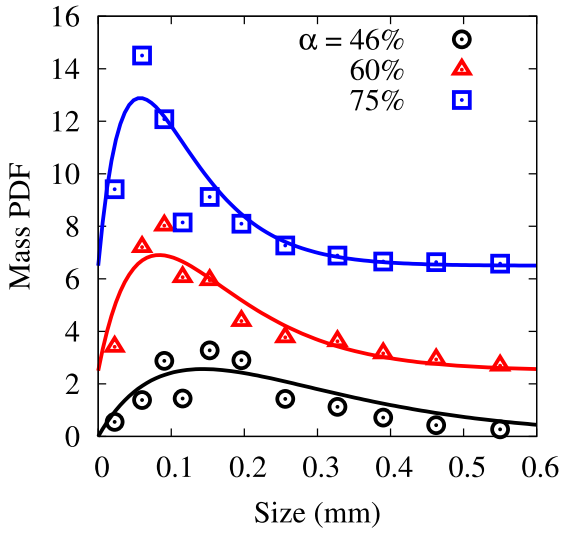

FIG. 8. Distribution of recovered fragments for the various porosity samples.

Final fragments are predominately formed by random cracks propagating across these lamellae, orthogonal to the original growth direction. The lamellar length is much larger than the final characteristic fragment size. If we assume the fragment distribution can be treated as an uncorrelated, Poisson process of cracks nucleating across a quasi-1D lamellar strip, it is reasonable to describe this process using a simple one-dimensional Lineau distribution.[23] The majority of lamellae in smaller fragments have failed at junction interfaces, and the main determinant of fragment size is thus the cracks propagating across the lamellar length. For characteristic fragment size μ and crack nucleation governed by Poisson statistics, the Lineau distribution gives the distribution of number of fragments over a linear size s as

$$n(s) = \frac{1}{\mu}\exp(-s/\mu). \tag{1}$$

A more suitable comparison for sieve data is the mass distribution over a linear size; in this case, the 1D Lineau distribution takes the form

$$m(s) = \left(\frac{s}{\mu^2}\right)\exp\left(-\frac{s}{\mu}\right). \tag{2}$$

The solid lines in Figure 8 are fits to the experimental data using Eq. (2) with the characteristic fragment size μ as a fit parameter. This form provides a good match to the experimental trend, and yields average fragment sizes μ of 57.6 μm, 83.5 μm, and 143.4 μm for the 75%, 60%, and 45% samples, respectively. We note that two- and three-dimensional analogs of the Lineau form are in considerably worse agreement with the collected fragment distribution. Other common particle size distributions for brittle materials such as the empirical Rosin-Rammler[24] and Gates-Gaudin-Schuhmann[25,26] forms are also able to fit the data. However, our goal here is to use a distribution with as few parameters as possible, and for which the parameters can be traced to a physical origin. The Lineau distribution provides a good fit to the experimental fragment sizes, is consistent with the fracture processes observed in recovered samples, and requires only a characteristic fragment size.

We next consider one of the main efforts in this manuscript, development of a model that can predict the average fragment size μ for these cellular alumina materials. We first assume that that during dynamic loading, all lamellae fail at junction interfaces, and that the measured fragmentation distribution is primarily related to crack initiation and merging across the lamellar width. A schematic of our model is given in Figure 9, where we assume tensile plane stress on the lamella during impact and a candidate cylindrical fragment of radius a within the lamella itself. We assume that the relevant kinetic energy for a candidate fragment is the motion relative to its center of mass. This local kinetic energy is balanced against two additional terms: first, the surface energy required to create N cylindrical fragments out of the lamella structure. Second, we must consider the strain energy as the lamella expands in tension; we assume that fragmentation begins at a critical stress σ_c which is related to the critical stress intensity factor for pre-existing microcracks in the lamella. This approach is in the spirit of classic fragmentation theories by Grady[23,27] and Glenn and Chudnovsky,[28] who treated fragmentation as a balance between kinetic, fracture, and strain energies. More recent numerical simulations such as those developed by Zhou *et al.*,[29] Paliwal and Ramesh,[30] and Levy and Molinari[31] have shown promise for predicting brittle fragmentation behavior, but generally require a level of understanding of material defects and mechanical response which is currently unavailable for the hierarchical freeze-cast structures we consider here.

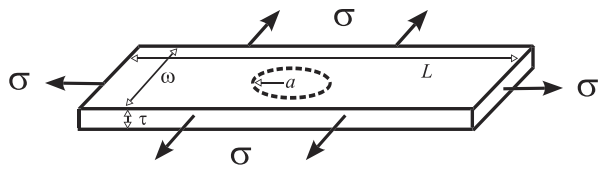

FIG. 9. Schematic of the energy balance model for a cylindrical fragment formed within a detached lamella.

We first consider the local kinetic energy T of the candidate fragment. A cylindrical shell at a distance r from the center of a candidate fragment has a mass of

$$dm = 2\pi\rho\tau r dr, \tag{3}$$

where ρ is the ceramic bulk density and τ is the lamellar thickness. Its kinetic energy can be written as

$$dT = \frac{1}{2}\dot{r}^2 dm, \tag{4}$$

where the expansion velocity $\dot{r}$ can be given in terms of a density expansion rate $\dot{\rho}$

$$\dot{r} = -\left(\frac{\dot{\rho}}{2\rho}\right)r.$$

The total kinetic energy of a collection of $N = L\omega/\pi a^2$ fragments in a lamella of length L is given as

$$T = N\int_o^a dT = \frac{1}{4}L\omega\tau\rho(\dot{\epsilon}a)^2, \tag{5}$$

where we have introduced the strain-rate, $\dot{\epsilon} = -\dot{\rho}/2\rho$. We assume, following Glenn and Chudnovsky,[28] that there is no residual strain remaining in the newly formed fragments after fracturing. Thus, the elastic strain energy available for fragmentation can be written

$$U = \frac{L\omega\tau}{E}\sigma_c^2(1-\nu), \tag{6}$$

where E is the Young's modulus of bulk alumina and ν is its Poisson's ratio. The lamella has been assumed to be in a condition of plane stress. Finally, we consider the change in surface energy when the lamella is broken into a collection of N cylindrical fragments. The initial surface energy is given by $\Gamma_i = S_a\gamma$, where γ is the specific surface energy $\gamma = K_{ic}^2/2\rho c^2$, and S_a is the total surface area of the unfractured lamella. The total residual surface energy Γ_{res} when N cylindrical fragments of radius a are formed is

$$\Gamma_{\text{res}} = N\Gamma_n = \frac{L\omega\gamma}{\pi a^2}(2\pi a\tau + 2\pi a^2). \tag{7}$$

The equilibrium fragmentation condition is given by a balance of these three energies

$$T + U + \Gamma_i = \Gamma_{\text{res}}. \tag{8}$$

Substituting the respective energy equations in gives the following cubic equation:

$$a^3 + \left[\frac{4\sigma_c^2(1-\nu)}{E\rho\dot{\epsilon}^2} + \frac{8\gamma}{L\rho\dot{\epsilon}^2} + \frac{8\gamma}{\omega\rho\dot{\epsilon}^2}\right]a - \frac{8\gamma}{\rho\dot{\epsilon}^2} = 0. \tag{9}$$

Solving Eq. (9) for the equilibrium fragment size a gives

$$a = \frac{\kappa - \beta^2}{\beta}, \tag{10}$$

where

$$\beta = \left(\lambda + \sqrt{\lambda^2 + \kappa^3}\right)^{\frac{1}{3}},$$

$$\lambda = -2\left(\frac{2K_{ic}}{\rho c\dot{\epsilon}}\right)^2,$$

$$\kappa = \frac{4}{3(\rho c\dot{\epsilon})^2}\left[\sigma_c^2(1-\nu) + K_{ic}^2\left(\frac{L+\omega}{L\omega}\right)\right].$$

We assume that the critical stress σ_c is equal to the tensile strength of the alumina material, which should be suitable in the case where widespread delamination occurs. The lamellar length L is very large compared to the average fragment size, and based on our observations it is comparable to our overall sample dimensions (16 mm). The other lamellar dimensions, the thickness τ and the width ω both decrease in a similar manner with increasing porosity (see Fig. 2). The ratio between them appears to be roughly constant in our recovered fragments, and thus we assume that $\omega/\tau = \xi$, where the constant ξ is approximately 20 for these ice-templated alumina structures. The strain rate at the lamellar level was estimated assuming a simple three-point bending deformation of a lamella

$$\dot{\epsilon} = \frac{6\tau v_s}{\omega^2}, \tag{11}$$

where v_s is the striker velocity determined based on the conservation of momentum of the impactor and the striker bar. The strain rate values derived from this equation were in the range of 10^4–10^5 depending on the microstructural parameters (note that velocity is constant in all experiments), which are reasonable values for dynamic loading on a microstructured lamella.

Table II presents the alumina material properties used in this model. The fracture toughness of fine-grained alumina varies with grain size, and a value of 3.5 MPa$\sqrt{\text{m}}$ was taken to be representative for the observed grain size in our lamellae.[32] The critical stress, as discussed above, is taken to be the tensile strength of bulk alumina at ambient conditions.[33]

TABLE II. Alumina material properties used in the fragmentation model. Properties taken from Refs. 32 and 33.

Property	Value
Bulk alumina density ρ	3.95 g/cm^3
Sound speed c	10.22 km/s
Fracture toughness K_{ic}	3.5 MPa$\sqrt{\text{m}}$
Poisson's ratio ν	0.231
Critical stress σ_c	267 MPa

With these parameters, we made use of the fragmentation model developed above to estimate the average fragment size of the freeze-cast specimens. Figure 10 shows the results of the above theory plotted as average fragment size against the lamellar width. For the samples synthesized in this study, the latter quantity has a direct relationship to porosity. The above theory produces average fragment sizes in very good agreement with experimental values, and successfully predicts the trend of increasing average fragment size with lamellar width. As the lamellar width increases, the average fragment size increases and eventually the curve flattens off at large ω due to the reduction in effective strain-rate. No samples synthesized here had a lamellar width above 600 μm, and thus we cannot fully validate whether the theory is in agreement over the full range. However, the experimental trend is that the thickness also increases as lamellar width increases, and as ω grows larger we will move out of a two-dimensional, plane stress condition and violate the basic assumptions of our model. With this caveat, it is encouraging that the above theory accurately predicts characteristic fragment sizes using only properties of bulk alumina, and also captures the changing trend as the morphology is altered.

We note that if the strain-rate is held constant, the variation of fragment size with ω is quite small. Most of the variation in Fig. 10 arises from the variation in strain rate with lamellar size, Eq. (11). Though the impact velocity in our

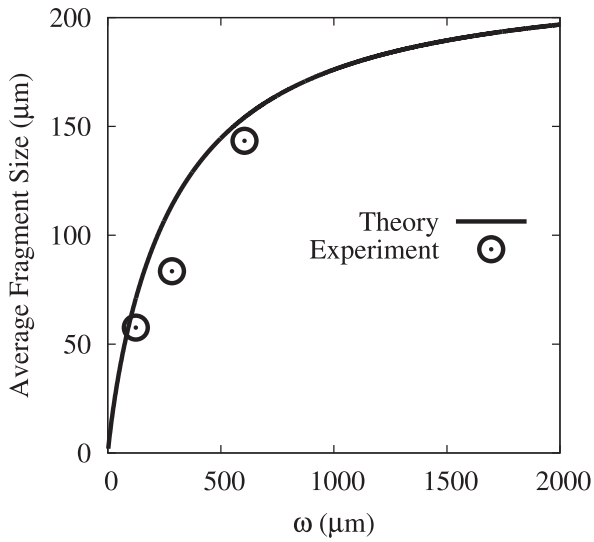

FIG. 10. Variation in average fragment size with lamellar width ω. Theoretical results from Eq. (10) are shown along with experimental values for each porosity of freeze-cast alumina scaffold studied here.

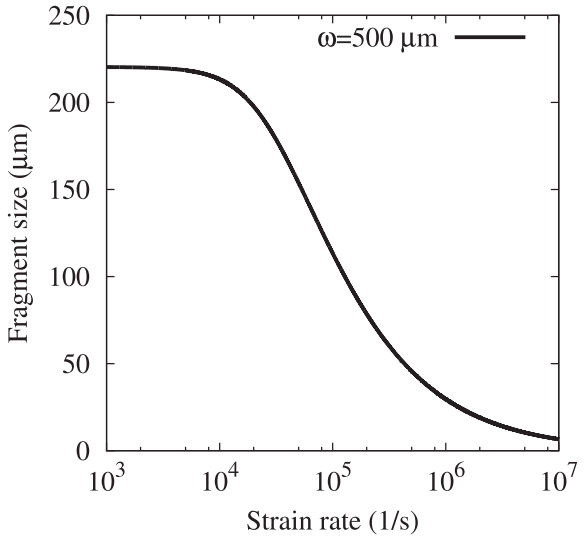

FIG. 11. Strain rate dependence of the average fragment size for a fixed lamellar width.

experiments is held constant, the strain-rate in our model still varies due to this dependence on lamellar dimensions. An explicit strain-rate variation of average fragment size is shown in Figure 11, with the microstructure values held constant at $\omega = 500\,\mu$m and $\xi = 20$. At the low end of the dynamic strain-rate regime, the fragment size plateaus at a rate-independent value, as expected when the strain energy is accounted for in the fragmentation energy balance.[28] This plateau is responsible for the leveling-off behavior seen in Figure 9 at large ω. With the exception of morphology-specific terms such as ξ that are specific to this freeze-cast material, we expect that a similar model could be applied to the fragmentation of any brittle, lamellar material.

IV. CONCLUSIONS

The microstructure and fragmentation behavior of ice-templated, freeze-cast alumina materials were studied as a function of varying sample porosity. The porosity of the material is a direct replica of the solvent content and can be carefully controlled; in addition to a porosity change, however, there are also a range of changes in the microstructure and lamellae comprising the material. Lamellar thickness and width in the freeze cast samples decrease significantly as the porosity of the material increases. Impact tests were performed to study the fracture under dynamic loading, and the general fracture trends are consistent across all porosities; both trans- and intergranular failure are observed, and all samples show nearly complete delamination and cracking across the lamellar width. Though all recovered fragment distributions are well described by a one-dimensional Lineau form, there is a systematic decrease in the characteristic fragment size of this Lineau distribution with increasing porosity. A theoretical model was developed to predict this average fragment size of a freeze cast alumina material, based on a balance of kinetic, strain, and surface energy. Using only properties of bulk alumina, the model correctly predicts the characteristic fragment sizes as well as the reduction in this characteristic size as the porosity increases. This approach allows one to predict the fragmentation behavior of the freeze-cast scaffolds from a small number of material properties.

ACKNOWLEDGMENTS

This work was funded by the Defense Threat Reduction Agency under the supervision of Bill Wilson. Freeze casting work at LLNL was performed through the AMEA collaboration fostered by the LLNL National Security Office. All LLNL work was performed under the auspices of the U.S. Department of Energy by Lawrence Livermore National Laboratory under Contract No. DE-AC52-07NA27344. Lawrence Livermore National Security, LLC.

[1]S. Deville, Adv. Eng. Mater. **10**, 155 (2008).
[2]M. C. Gutierrez, M. L. Ferrer, and F. del Monte, Chem. Mater. **20**, 634 (2008).
[3]L. Qian and H. F. Zhang, J. Chem. Technol. Biotechnol. **86**, 172 (2011).
[4]W. L. Li, K. Lu, and J. Y. Walz, Int. Mater. Rev. **57**, 37 (2012).
[5]M. M. Porter, J. Mckittrick, and M. A. Meyers, JOM **65**, 720 (2013).
[6]S. Deville, E. Saiz, R. K. Nalla, and A. P. Tomsia, Science **311**, 515 (2006).
[7]E. Munch, M. E. Launey, D. H. Alsem, E. Saiz, A. P. Tomsia, and R. O. Ritchie, Science **322**, 1516 (2008).
[8]U. G. K. West, M. Schecter, A. E. Donius, and P. M. Hunger, Philos. Trans. R. Soc., A **368**, 2099 (2010).
[9]S. Deville, E. Saiz, and A. P. Tomsia, Biomaterials **27**, 5480 (2006).
[10]M. E. Launey, E. Munch, D. H. Alsem, H. B. Barth, E. Saiz, A. P. Tomsia, and R. O. Ritchie, Acta Mater. **57**, 2919 (2009).
[11]M. E. Launey, E. Munch, D. H. Alsem, E. Saiz, A. P. Tomsia, and R. O. Ritchie, J. R. Soc., Interface **7**, 741 (2010).
[12]B. H. Yoon, W. Y. Choi, H. E. Kim, J. H. Kim, and Y. H. Kim, Scr. Mater. **58**, 537 (2008).
[13]J. Han, L. Hu, Y. Zhang, and Y. Zhou, J. Am. Ceram. Soc. **92**, 2165 (2009).
[14]S. Deville, Materials **3**, 1913 (2010).
[15]E. Munch, E. Saiz, A. P. Tomsia, and S. Deville, J. Am. Ceram. Soc. **92**, 1534 (2009).
[16]J. W. Moon, H. J. Hwang, M. Awano, and K. Maeda, Mater. Lett. **57**, 1428 (2003).
[17]A. Macchetta, I. G. Turner, and C. R. Bowen, Acta Biomater. **5**, 1319 (2009).
[18]H. Bai, F. Walsh, B. Gludovatz, B. Delattre, C. Huang, Y. Chen, A. P. Tomsia, and R. O. Ritchie, Adv. Mater. **28**, 50–56 (2015).
[19]M. M. Porter, M. Yeh, J. Strawson, T. Goehring, S. Lujan, P. Siripasopsotorn, M. A. Meyers, and J. McKittrick, Mater. Sci. Eng., A **556**, 741 (2012).
[20]F. Bouville, E. Portuguez, Y. Chang, G. L. Messing, A. J. Stevenson, E. Maire, L. Courtois, and S. Deville, J. Am. Ceram. Soc. **97**, 1736 (2014).
[21]See supplementary material at http://dx.doi.org/10.1063/1.4939702 for additional SEM images.
[22]P. L. Swanson, C. J. Fairbanks, B. R. Lawn, Y. W. Mai, and B. J. Hockey, J. Am. Ceram. Soc. **70**, 279 (1987).
[23]D. E. Grady, *Fragmentation of Rings and Shells* (Springer-Verlag, Berlin, 2006).
[24]P. Rosin and E. Rammler, J. Inst. Fuel **7**, 29 (1933).
[25]A. O. Gates, Trans. AIME **52**, 875 (1915).
[26]R. Schuhmann, Technical Report Publication No. 1189, American Institute of Mining and Metallurgical Engineers, New York, NY (1940).
[27]D. E. Grady, J. Appl. Phys. **53**, 322 (1982).
[28]L. A. Glenn and A. Chudnovsky, J. Appl. Phys. **59**, 1379 (1986).
[29]F. Zhou, F. Molinari, and K. T. Ramesh, Int. J. Fract. **139**, 169 (2006).
[30]B. Paliwal and K. Ramesh, J. Mech. Phys. Solids **56**, 896 (2008).
[31]S. Levy and J. F. Molinari, J. Mech. Phys. Solids **58**, 12 (2010).
[32]A. Muchtar and L. Lim, Acta Mater. **46**, 1683 (1998).
[33]R. G. Munro, J. Am. Ceram. Soc. **80**, 1919 (1997).